Super-resolution microscopy localizes perilipin 5 at lipid droplet-mitochondria interaction sites and at lipid droplets juxtaposing to perilipin 2

BBA - Molecular and Cell Biology of Lipids 1863 (2018) 1423–1432

Contents lists available at ScienceDirect

BBA - Molecular and Cell Biology of Lipids

journal homepage: www.elsevier.com/locate/bbalip

Super-resolution microscopy localizes perilipin 5 at lipid droplet-mitochondria interaction sites and at lipid droplets juxtaposing to perilipin 2

Anne Gemmink[a,b], Sabine Daemen[a,b], Helma J.H. Kuijpers[c], Gert Schaart[a,b], Hans Duimel[c], Carmen López-Iglesias[c], Marc A.M.J. van Zandvoort[d,e,f], Kèvin Knoops[c], Matthijs K.C. Hesselink[a,b,*]

[a] Department of Nutrition and Movement Sciences, Maastricht University Medical Centre+, 6200 MD Maastricht, the Netherlands
[b] NUTRIM School for Nutrition and Translational Research in Metabolism, Maastricht, the Netherlands
[c] Microscopy Core Lab, FHML and M4I Maastricht Multimodal Molecular Imaging Institute, Maastricht University, 6200 MD Maastricht, the Netherlands
[d] Department of Genetics & Cell Biology – Molecular Cell Biology, Maastricht University Medical Centre+, 6200 MD Maastricht, the Netherlands
[e] CARIM – Cardiovascular Research Institute Maastricht, Maastricht, the Netherlands
[f] Institute for Molecular Cardiovascular Research IMCAR, Universitätsklinikum, Aachen, Pauwelstrasse 30, Aachen, Germany

ARTICLE INFO

Keywords:
Perilipin 5
Perilipin 2
Lipid droplets
Skeletal muscle
Mitochondria
Super-resolution microscopy

ABSTRACT

Objective: Intramyocellular lipid droplets (LD) and their coat proteins PLIN2 and PLIN5 are involved in lipolysis, with a putative role for PLIN5 in mitochondrial tethering. Reportedly, these proteins co-localize and cover the surface of the LD. To provide the spatial basis for understanding how these proteins possess their distinct roles, we examined the precise location of PLIN2 and PLIN5 and explored PLIN5 presence at LD-mitochondria contact sites using Stimulated emission depletion (STED) microscopy and correlative light-electron microscopy (CLEM) in human skeletal muscle sections.

Methods: LDs were stained by MDH together with combinations of mitochondrial proteins and PLINs. Subcellular distribution and co-localization of PLIN proteins and mitochondria was imaged by STED microscopy (Leica TCS SP8) and quantified using Pearson's correlation coefficients and intensity profile plots. CLEM was employed to examine the presence of PLIN5 on mitochondria-LD contact sites.

Results: Both PLIN2 and PLIN5 localized to the LD in a dot-like, juxtaposed fashion rather than colocalizing and covering the entire LD. Both STED and CLEM revealed a high fraction of PLIN5 at the LD-mitochondria interface, but not at mitochondrial cristae, as suggested previously.

Conclusion: Using two super-resolution imaging approaches, this is the first study to show that in sections of human skeletal muscle PLIN2 and PLIN5 localize to the LD at distinct sites, with abundance of PLIN5 at LD-mitochondria tethering sites. This novel spatial information uncovers that PLIN proteins do not serve as lipolytic barriers but rather are docking sites for proteins facilitating selective lipase access under a variety of lipolytic conditions.

1. Introduction

Virtually all eukaryotic cell types can store fat in cellular lipid droplets (LDs). In muscle, stored fat is dispersed throughout the myofibers in droplets ranging in size and subcellular location in a muscle fiber type specific fashion [1]. Total muscle fat content correlates with insulin resistance, a hallmark for type 2 diabetes development. Data from endurance trained athletes [2,3] and from diet and training intervention studies (for review see e.g., Daemen et al. [4]) seem to suggest that storage of muscle fat in LDs that are highly dynamic does not impede with insulin sensitivity. The dynamic nature of LDs requires the interaction of LDs with proteins involved in LD turnover (the continuous process of lipid synthesis and hydrolysis). In addition, the potential of LDs to sequester bioactive (insulin desensitizing) lipid moieties seems to alleviate the lipotoxic effects of lipids to insulin sensitivity [1]. Thus, it is of direct clinical relevance to have a detailed understanding of how myocellular LDs interact with proteins involved in LD lipolysis, or in directing (bio-active) lipid moieties to oxidation or storage.

Confocal immunofluorescence microscopy revealed muscle-fiber

* Corresponding author at: Department of Nutrition and Movement Sciences, NUTRIM School for Nutrition and Translational Research in Metabolism, Maastricht University Medical Centre+, 6200 MD Maastricht, the Netherlands.
E-mail address: Matthijs.hesselink@maastrichtuniversity.nl (M.K.C. Hesselink).

https://doi.org/10.1016/j.bbalip.2018.08.016
Received 6 June 2018; Received in revised form 6 August 2018; Accepted 29 August 2018
Available online 31 August 2018
1388-1981/

type specific differences in coating of myocellular LDs with PLIN2 and PLIN5, proteins of the perilipin family [5–7]. Furthermore, confocal and widefield immunofluorescence microscopy suggests that PLIN2 and PLIN5 envelop myocellular lipid droplets in an unremitting labeling pattern [5,8–10], indicative of co-localization of PLIN2 and PLIN5. Although PLIN2 and PLIN5 both are involved in LD lipolysis, PLIN2 appears to shield the LD from lipolysis by hindering interaction of the major triacylglycerol lipase ATGL [11] while PLIN5 appears to regulate PKA-mediated increased lipolysis by actively recruiting multiple lipolytic players to the LD surface [12,13]. Thus, PLIN5 (co)regulates elevated lipolysis to fuel fat oxidation in periods of increased myocellular energy demand. In support of this notion, we observed a tight correlation between PLIN5 content in muscle homogenates and mitochondrial respiration on a lipid derived substrate, an association that was absent for PLIN2 [14]. Moreover, PLIN5 and mitochondrial marker proteins seem to co-localize when using widefield fluorescence microscopy. An observation that was confirmed using protein-A based immunogold electron microscopy (IEM) [14], and which was not made for PLIN2. It has been shown that tethering of LDs and mitochondria requires the final 20 C-terminal amino acids of PLIN5 [12], suggesting a role for PLIN5 in promoting LD mitochondrial interaction. Somewhat surprisingly, our IEM also revealed PLIN5-derived signal on mitochondrial cristae [14], suggesting import of the PLIN5 protein into the mitochondrial inner-membrane.

These clear distinct roles of PLIN2 and PLIN5 in LD dynamics suggest a distinct spatial distribution of these proteins, rather than what is indicated by images showing that PLIN2 and PLIN5 are enveloping the LDs. For a better understanding of how LDs and LD dynamics interact with insulin sensitivity, detailed spatial information of the location of PLIN2 and PLIN5 at the LD surface, and the putative location of PLIN5 to mitochondria is needed. In addition, the PLIN5 association with the mitochondrial cristae, which we reported previously [14] has not been confirmed by others [15] or solidly established, hence requires further examination. Thus, the aim of the present study is threefold;

a. to examine PLIN2 and PLIN5 localization on the LD.
b. to study the hypothesis that in human skeletal muscle PLIN5 locates at the LD-mitochondrial interface.
c. to examine if location of PLIN5 to the mitochondrial cristae observed by IEM can be confirmed using other modes of microscopy.

To achieve these aims, we took advantage of recent developments in super-resolution microscopy. With stimulated emission depletion (STED) microscopy one can image well below the diffraction limit of light microscopy [16–18] down to lateral resolution of 60 nm [19]. This gives detailed information about the precise location of proteins on organelles, which contributes to understanding their function. This is particularly useful, when examining human tissue slides, where the proteins of interest cannot readily be genetically manipulated.

2. Methods

2.1. Experimental model and subject details

To identify and test a probe suitable to image LDs in muscle tissue sections along with STED-based imaging of related proteins, m. tibialis anterior samples of 12-week old male ZDF rats were used. These samples were obtained from a previously performed study which was approved by the institutional Animal Care and Use Committee of Maastricht. For the combined confocal imaging of LDs with two-color STED imaging, muscle biopsies were used from the m. vastus lateralis of multiple male volunteers (age range: 24–61 years) from previously performed studies approved by the institutional Medical Ethical Committee in which these subjects signed an informed consent. In samples derived from rats as well as the human muscle samples, fat and blood were removed and samples were immediately frozen in melting isopentane (2-methyl butane) and stored at −80 °C. Five μm thick sections were cut and mounted on glass slides.

2.2. Method details

2.2.1. Staining procedures

2.2.1.1. Dual labeling of LDs with Bodipy and MDH. Based upon the reported spectral properties and its photo-stability we chose to test monodansylpentane (MDH; SM1000a, Abgent, San Diego, USA) as a LD dye. This dye permits reliable investigation of dynamic LD regulation within living cells using fluorescence microscopy [20], but has not yet been applied to muscle sections and has not been tested for interference with STED specific dyes.

Five μm thick sections were cut and fixed with 3.7% formaldehyde (Merck, Darmstadt, Germany) in PBS for 30 min and treated with 0.25% Triton X-100 (TX100, Merck, Darmstadt, Germany) in PBS for 5 min. To identify individual cells, the sections were incubated with a primary antibody against laminin (L9393, Sigma, St. Louis, USA) diluted 1:25 in 0.05% Tween20 (Sigma, St. Louis, USA) in PBS for 1 h. Sections were washed and incubated for 1.5 h at 37 °C with Bodipy 493/503 (D3922, Molecular Probes, Leiden, The Netherlands) 1:100, MDH 1:1000 and the appropriate conjugated secondary antibody AlexaFluor555 (AF555) (Invitrogen, Groningen, The Netherlands). After washing, sections were mounted with Mowiol (Merck, Darmstadt, Germany) and covered with #1.5 coverslips.

2.2.1.2. Immunohistochemistry for combined confocal and two-color STED imaging. Five μm thick sections were cut and fixed for 30 min with 3.7% formaldehyde/PBS. Subsequently, sections were blocked in 1% BSA (Sigma, St. Louis, USA) in PBS for 45 min and treated with 0.25% TX100/PBS for 5 min. Primary antibodies against PLIN5 (GP31, Progen, Heidelberg, Germany), TOMM20 (ab56783, Abcam, Cambridge, UK), PLIN2 (03-610102, American Research Products, Oxfordshire, UK), and/or OXPHOS (ab110411, Abcam, Cambridge, UK) were used and incubated for 1 h. This was followed by incubation with MDH 1:1000, and the appropriate conjugated secondary antibodies AF488 (Invitrogen, Groningen, The Netherlands) and Abberior Star 440SX (AS440) (Sigma, St. Louis, USA) for 1 h at 37 °C. Sections were mounted with Mowiol and covered with #1 coverslips.

2.2.1.3. Staining procedure for CLEM experiments. Human muscle tissue was chemically fixed with a mixture of 2% paraformaldehyde and 0.1% glutaraldehyde in PHEM (240 mM PIPES, 100 mM HEPES, 40 mM EGTA and 8 mM Magnesium Sulphate Heptahydrate) buffer at 4 °C. After washing with 50 mM glycine in PHEM, the tissue was embedded in 12% gelatine and infiltrated with 2.3 M sucrose. Mounted gelatine blocks were frozen in liquid nitrogen. Thin sections of 60 nm thick were cut in an ultra cryo-microtome (Leica EM Ultracut UC6, Vienna, Austria) and collected with 2% methylcellulose in 2.3 M sucrose and 50 mesh formvar-coated Cu grid. All incubations were performed at room temperature unless stated otherwise. Grids were placed on a 2% gelatin in PB plate for 10 min at 37 °C. Sections were incubated 2 × 5 min with 0.15% Glycine in PHEM. Subsequently sections were washed with 1% BSA in PHEM for 5 min. First antibodies (PLIN5 1:50; Laminin 1:50; OXPHOS 1:25 in 1% BSA in PHEM) were applied for 1 h. Sections were washed 4 × 5 min with 1% BSA in PHEM and subsequently incubated for 1 h with appropriately conjugated secondary antibodies (AlexaFluor405, AlexaFluor488 and AlexaFluor555) all diluted 1:200 in 1% BSA in PHEM. Sections were washed 2 × 5 min with 1% BSA in PHEM and subsequently 6 × 5 min with PHEM. After staining for STED imaging, grids were sandwiched between an object glass and a coverslip. A 20 μl drop of PHEM was placed on the object glass. The grid with the section on top (the section will be on the side of the coverslip) was put into the drop of PHEM. Subsequently, the drop of PHEM with grid was sealed off with a coverslip which was first placed on a lid with grease. This grease seals

the drop of PHEM and prevents dehydration of the sample.

After STED imaging, the coverslip was removed and the grid with sample was quickly dried on a filter paper. Grids were washed 2 × 5 min with PHEM and subsequently incubated with 1% glutaraldehyde in PHEM for 5 min. PHEM was applied on the grids for 2 × 5 min followed by 6 × 1 min of H_2O. Sections were incubated with methyl cellulose and uranyl acetate for 3 × 5 s followed by a single 10-min incubation at 4 °C. Grids were dried and stored until imaging with transmission electron microscopy (TEM).

2.2.2. Imaging procedures

2.2.2.1. Confocal imaging of LDs. Sections were imaged on a Leica TCS SP8 STED microscope using the confocal mode with a 63× oil immersion/1.4 N.A. objective using a 1.1 optical zoom. Images of 2048 × 2048 pixels were obtained, resulting in a pixel size of 82 × 82 nm. For imaging MDH, a 405 nm laser line was used and emission was collected at 415–460 nm. A white light laser (range 470 nm–670 nm) was used to image Bodipy 493/503 and laminin-AF555. To excite Bodipy 493/503 and laminin-AF555 wavelengths of 488 nm and 555 nm were used, while emission was collected at 500–530 nm and 565–650 nm, respectively. Emission was detected with a PMT detector. Gain and off-set were set at values which prevented saturated and empty pixels. After image acquisition, images were deconvolved using Huygens Professional Software (Scientific Volume Imaging B.V., Hilversum, the Netherlands).

2.2.2.2. STED imaging of LDs and related proteins. To acquire STED images, a Leica TCS SP8 STED microscope was used with a 100×/1.4 N.A. orange objective. Images consisted of 1024 × 1024 pixels and a 5× optical zoom was used, resulting in a pixel size of 23 × 23 nm. Both the white light laser and the 592 nm depletion laser are pulsed and were aligned before use to get an optimal STED result. LDs were imaged in the confocal modus as described above based upon the MDH derived signal. The combinations PLIN5-AF488/TOMM20-AS440, PLIN5-AF488/OXPHOS-AS440, PLIN5-AF488/PLIN2-AS440, and OXPHOS-AF488/TOMM20-AS440 were imaged using STED. AS440 and AF488 were excited with a wavelength of 470 nm and 514 nm, respectively. The combination of excitation wavelength intensity and gain was set such to prevent pixel saturation. Emission was detected with a hybrid detector and collected between 480 and 500 nm for AS440 and between 535 and 550 nm for AF488. The intensity of the STED laser was empirically set at 29.5% to obtain proper spatial resolution improvements, but preventing bleaching of the fluorophores. Images were obtained using a pixel dwell time of 100 ns. Only photons with a lifetime between 0.3 and 6.0 ns were collected (gating). In addition, a pinhole of 0.9 Airy Unit was used. For comparing confocal and STED microscopy, the combination OXPHOS-AF488/TOMM20-AS440 was also imaged in confocal mode. Confocal imaging took place at the same spot and with the same settings as used for STED microscopy, but with the STED laser turned off. All images were deconvolved with Huygens Professional Software (Scientific Volume Imaging B.V., Hilversum, The Netherlands) using the deconvolution express modus after checking all parameters.

2.2.2.3. CLEM experiments. First an overview image of the grid was acquired with the 25×/0.95 N.A. water objective in the bright field modus. In this image the approximate location of the STED image was marked and was used to find the imaged muscle fiber on the TEM quickly. STED imaging was performed with a 100×/1.4 N.A. oil objective. In addition, an overview image (no zoom) in confocal mode only was taken of Laminin-AF405, PLIN5-AF488 and OXPHOS-AF555. Excitation wavelengths used were respectively 405 nm, 488 nm and 555 nm. Emission was detected at 415–460 nm, 500–550 nm and 565–625 nm for respectively Laminin-AF405, PLIN5-AF488 and OXPHOS-AF555. Subsequently a high detailed image was obtained at 5× zoom. This detailed image consisted a combined confocal (Laminin-AF405 and OXPHOS-AF555) and STED (PLIN5-AF488). To prevent any bleaching of the AF555 by the STED laser (592 nm), a sequential image was taken. The first sequence contained all the confocal imaging and the second sequence the STED imaging of PLIN5. The same excitation and emission wavelengths as for the overview image were used. The STED laser was used at 29.5% laser intensity. Both the overview and detailed images consisted of multiple z-slices from which a maximal intensity projection was made in ImageJ [21].

After STED imaging, samples were prepared for the FEI T12 transmission electron microscope as described above. Based on the grid and confocal overview image taken by confocal microscopy the same cell was searched back inside the TEM. Images were acquired at 120 kV with a FEI Eagle CCD camera. First a low resolution overview image was taken for initial image alignment. Subsequently a high-resolution 20 k × 20 k image mosaic was acquired with a pixel size of 1.66 nm using the MyMesh software and reconstructed to one large high-resolution image using MyStitch [22].

2.3. Quantification and statistical analysis

2.3.1. Colocalization analysis of confocal and STED images

To test whether MDH can be used for LD labeling in human skeletal muscle sections, images with a dual labeling with MDH and Bodipy 493/503 were analyzed in ImageJ by determining the Pearson's correlation coefficient with the Manders Coefficients plugin [23]. Before performing colocalization analysis, images were background corrected. The analyses were performed in several regions in each image to prevent any effect of imaging/staining artifacts. Pearson's correlation coefficient analysis was also performed to test whether STED is better suitable to spatially resolve proteins in near proximity than confocal imaging. Thus, we also examined if STED microscopy has sufficient resolving power to discriminate proteins at the inner (OXPHOS-AF488, antibody cocktail against all five respiratory electron transport chain complexes) and outer (TOMM20-AS440) mitochondrial membrane. The same colocalization analyses were performed on STED images of PLIN5-AF488/TOMM20-AS440, and PLIN5-AF488/OXPHOS-AS440. To examine the spatial distribution of PLIN2 and PLIN5 at the LD surface, intensity profile plots were created based upon manually drawn outer contours of individual LDs. The same was done for the combined MDH and Bodipy 493/503 staining. To put the observed Pearson's correlation coefficients into perspective we performed a couple of positive and negative controls. For the positive control for protein-protein colocalization we analyzed the Pearson's correlation coefficients for OXPHOS labeled with generic IgG secondary antibodies (Alexa Fluor 488 and Abberior Star 440) or with IgG specific isoforms (Alexa Fluor 488 IgG_1 and Alexa Fluor 555 IgG_{2a}). In addition, we double stained LDs for MDH and Bodipy 493/503 as a positive control. For negative controls we analyzed Pearson's correlation coefficients for Laminin and PLIN2, two proteins that do not colocalize at all. In addition, we performed this analysis on the same MDH-Bodipy images, but rotated the Bodipy channel 180 degrees, which would reflect random colocalization.

2.3.2. Aligning STED and TEM images

To examine whether PLIN5 is present in the mitochondria and/or at the LD-mitochondrion interface STED images and TEM images were aligned using the ec-CLEM plugin [24] in Icy [25]. The workflow for aligning the STED and TEM image is shown in Supplemental Fig. S2. First the overview images acquired with confocal and TEM were aligned based on cell membranes and mitochondria resulting in the first CLEM overview image. Subsequently the high detailed combined confocal and STED image of respectively OXPHOS and PLIN5 was aligned with this CLEM overview image based on the OXPHOS immunofluorescence staining present in both images. This resulted in a second CLEM overview image. Subsequently, this second CLEM overview image was aligned with the high resolution 10 × 10 stitched TEM image based on morphological characteristics present in both TEM

images (overview and high-resolution stitched TEM), resulting in a high-resolution CLEM image containing PLIN5 imaged by STED, OXPHOS imaged by confocal, and the mitochondria, LDs and contractile elements imaged at high-resolution by TEM.

2.3.3. Statistical analysis

Results of the Pearson's correlation coefficients are presented as mean ± SD. For statistical testing SPSS, version 21.0 (IBM Corp., Armonk, NY, USA) was used. A paired *t*-test was performed to test whether the Pearson's correlation coefficient obtained with confocal imaging was significant different from the Pearson's correlation obtained with STED imaging. A one-way ANOVA with a Bonferroni post-hoc test was performed to statistically compare the Pearson's correlation coefficients of the positive controls and the negative controls. A p-value < 0.05 was considered to be statistically significant.

3. Results

3.1. MDH as a blue lipid droplet dye in skeletal muscle

Currently available LD dyes emit green or red light and are excited by either the excitation wavelengths used for the STED probes (470 nm and 518 nm) or by the depletion laser (592 nm). In a one-depletion laser system like ours, these LD dyes will interfere with STED probes or with the depletion laser. As LDs are relatively large, STED microscopy is not required for imaging LDs. Thus, LDs can theoretically be imaged with a blue LD dye without interference with STED probes. MDH is a commercially available blue LD dye, used in cell cultures [20], yeast [26] and fixed fruit flies [27] only. We developed a protocol to visualize LDs in skeletal muscle sections by MDH and tested this against the widely used Bodipy 493/503. MDH stains LDs in skeletal muscle tissue in a pattern that upon visual inspection was similar to the Bodipy 493/503 signal (Fig. 1A) and upon quantification resulted in a high Pearson's correlation coefficient (0.842 ± 0.057, mean ± SD, Fig. 1B). The co-localization of the MDH and Bodipy 493/503- derived signal was further substantiated by intensity profile plots, showing peaks for MDH and Bodipy in the same pixels (Fig. 1C). Theoretically, these markers of co-localization can originate from bleed through of the Bodipy 493/503 signal into the blue (MDH) channel. To rule out this option, we co-stained MDH-labeled LDs along with PLIN2 as a LD coat protein using a secondary antibody emitting green light of similar wavelength as Bodipy493/503. Clearly, this combined staining showed LDs with and without PLIN2-derived signal (Fig. 1D), indicating we can image these channels without major bleed-through. As negative controls and to value the high Pearson's correlation coefficient for MDH and Bodipy 493/503 (see Supplemental Fig. S1), we computed the Pearson's correlation coefficient for the LD coat protein PLIN2 and the basement membrane marker laminin (supposed to stain completely different cell areas) resulting in a coefficient of −0.091 ± 0.031 (mean ± SD). Moreover, we re-computed the Pearson's correlation coefficient of Bodipy and MDH upon 180 degrees rotation of the Bodipy image, resulting in a coefficient of −0.218 ± 0.065 (mean ± SD, Supplemental Fig. S1). Jointly, these data clearly indicate that MDH is a STED-compatible valid LD dye detecting LDs in skeletal muscle sections similarly well as the classical Bodipy 493/503 dye.

3.2. Two-color STED imaging of near proximity mitochondrial proteins in human skeletal muscle

By immunogold electron microscopy (protein-A gold) we previously observed localization of PLIN5 at the mitochondrial outer membrane as well as at mitochondrial cristae [14], an observation that could not be confirmed by others using other methodology [15]. Therefore, we wanted to test if these observations could be confirmed using technology that is not depending on protein-A gold, like immunofluorescence-based STED microscopy. Thus, we need to show that the resolution of our super-resolution microscopy set-up suffices to spatially separate recognized outer-mitochondrial membrane proteins from proteins known to sit in the inner-mitochondrial membrane. Therefore, we used an antibody cocktail against individual structural components of all 5 respiratory chain complexes as a marker of inner-mitochondrial membrane proteins (OXPHOS) and translocase of the outer-mitochondrial membrane 20 (TOMM20) as an outer mitochondrial membrane protein. Imaging of these proteins in the confocal mode of our STED system, falsely suggests a high degree of co-localization (Fig. 2A, confocal panels and Fig. 2B Pearson's correlation plot and bar graph, coefficient: 0.657 ± 0.136, mean ± SD). As anticipated and by design of the equipment, the images captured in the STED mode possess strikingly better spatial resolution than images captured in the confocal mode, permitting making the distinction between the location of outer-mitochondrial membrane proteins (TOMM20) and inner-mitochondrial membrane proteins (OXPHOS) (Fig. 2A STED panels, Fig. 2B correlation plot and bar graph, Pearson's coefficient: 0.189 ± 0.173, mean ± SD; $p < 0.001$ vs. confocal).

These data indicate that our STED set-up permits making the distinction between outer-mitochondrial membrane proteins vs. proteins that associate with the inner-mitochondrial membrane. Thus, our STED microcopy set-up can be used to examine if the LD coat protein PLIN5 also localizes to outer- and/or inner-mitochondrial membrane.

3.3. PLIN5 is present at the mitochondrion-lipid droplet interface

PLIN5 has been observed at the LD surface as well as at LD-mitochondria interaction sites [12,14]. Using Tokuyasu-based immunogold (protein A-gold) electron microscopy, we showed that PLIN5 was also associated with the mitochondrial inner-membrane [14]. To substantiate these laborious EM-based findings in another system, we applied STED microscopy on human skeletal muscle sections stained for PLIN5 and OXPHOS or TOMM20. Strikingly, co-staining of PLIN5 and the OXPHOS proteins (Fig. 3A) shows PLIN5 presence in proximity of mitochondria, but does not support the previous IEM-based findings of PLIN5 being present at the cristae of the mitochondria (Pearson's correlation coefficient of PLIN5 with OXPHOS 0.208 ± 0.153, mean ± SD, Fig. 3A). Next, we examined if PLIN5 was located directly to the mitochondrial outer-membrane. Although, some of the PLIN5 was present in direct vicinity of the TOMM20 derived signal (Fig. 3B), co-localization according to Pearson's, was minimal (Fig. 3B, Pearson's correlation coefficient of PLIN5 with TOMM20 0.185 ± 0.159, mean ± SD). To put a low Pearson's correlation coefficient into perspective, we also computed the Pearson's correlation coefficient for a variety of positive controls. In skeletal muscle mitochondria complex I, III and IV can form supercomplexes [28]. We used an OXPHOS antibody cocktail detecting structural components in all 5 electron transport chain complexes, this cocktail contains different IgG isoforms. First, we used the generic IgG antibodies AF488 and AS440. These secondary antibodies theoretically bind competitively to all the primary antibodies in the cocktail which represent the spatially very closely related Complex I-V in the inner mitochondrial membrane. This positive control resulted in a Pearson's correlation coefficient of 0.696 ± 0.045 (Supplemental Fig. 1). A similar coefficient (0.740 ± 0.044, Supplemental Fig. 1) was obtained when using IgG subtype specific secondary antibodies ($IgG_1$to detect complex I and III and IgG_{2a} to detect complex II and IV). The highest Pearson's correlation coefficient we observed was not when staining different proteins or staining the same protein with different secondary antibodies, but upon examining two different lipid soluble dyes on the same lipid droplet (double staining of lipid droplets using Bodipy 493/503 and MDH), resulting in a Pearson's coefficient of 0.842 ± 0.057. All these Pearson's correlation coefficients were significantly higher than the correlation coefficients obtained with STED microscopy for OXPHOS/PLIN5 and TOMM20/PLIN5 ($p < 0.001$, Supplemental Fig. 1), indicating that PLIN5 does not co-localize with OXPHOS or TOMM20.

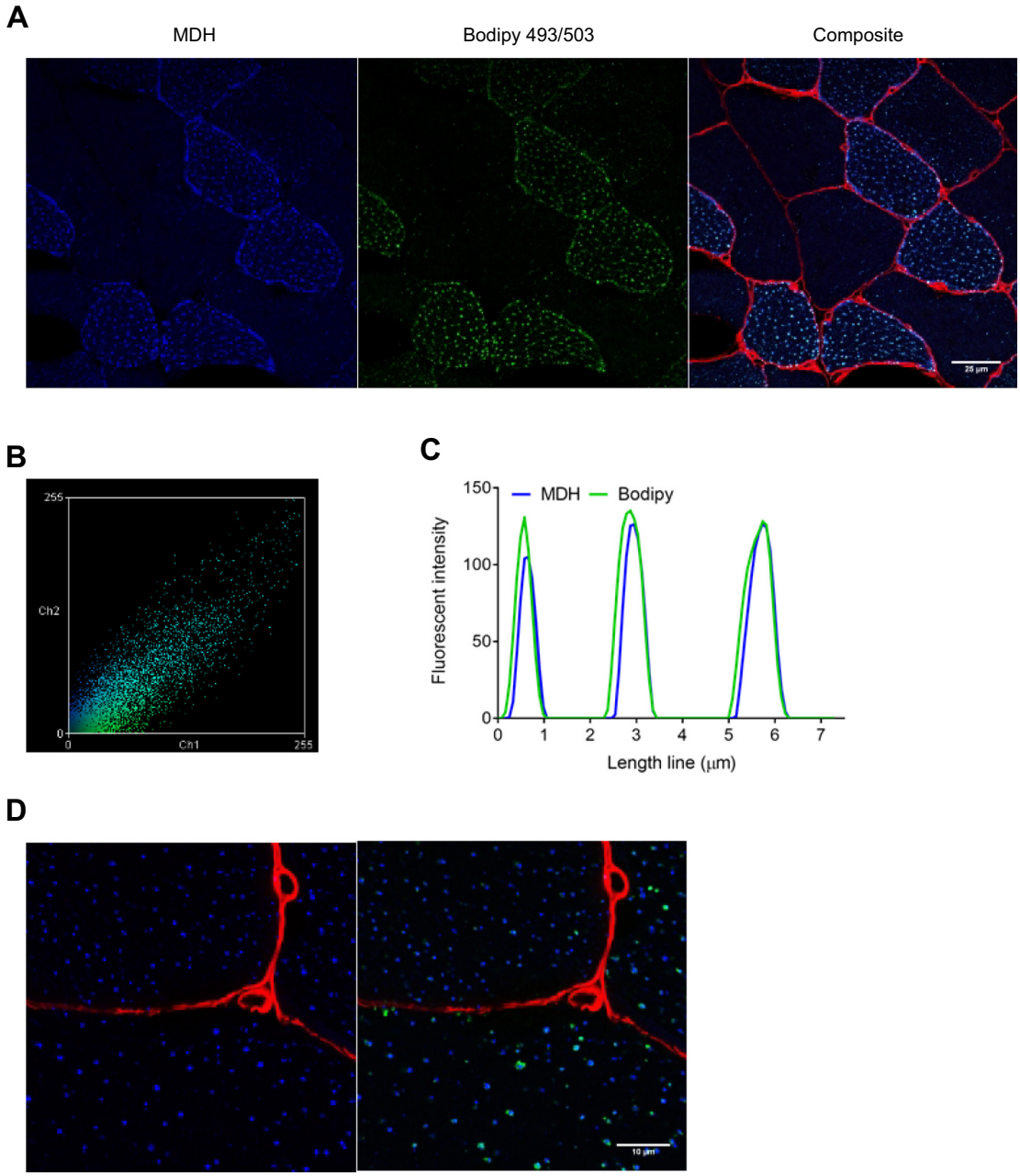

Fig. 1. MDH as a blue lipid droplet dye in skeletal muscle sections. (A) Co-staining of MDH and Bodipy 493/503 in ZDF rat m. tibialis anterior to test specificity of MDH as a blue LD dye in skeletal muscle sections. Right panel shows the merged confocal laser scanning image of MDH (blue), Bodipy 493/503 (green), and Laminin-AF555 (red). Middle and left panel show the individual channels of Bodipy 493/503 and MDH. (B) Plot of Pearson's correlation of pixel intensities of MDH and Bodipy 493/503, indicating that staining with Bodipy 493/503 or MDH results to a large extent in identification of the same lipid droplets. In the correlation plot Ch1 represents Bodipy493/503 and Ch2 represents MDH. The Pearson's correlation coefficient of Bodipy 493/503 and MDH and negative controls are shown in Supplemental Fig. S1. (C) Intensity plots of Bodipy 493/503 (green) and MDH (blue) along a line drawn through three lipid droplets. Each peak represents a LD. The overlapping peaks indicates that Bodipy 493/503 and MDH are staining the same LDs. (D) Confocal laser scanning image showing that MDH also stains lipid droplets in human skeletal muscle sections, MDH (blue) and Laminin-AF555 (red), left panel. In the right panel PLIN2 is shown in green and is only present at the LD surface, confirming that MDH stains LDs.

Although mitochondrial inner-membrane proteins (like proteins in the electron transport chain as shown in Fig. 3A) can be detected with STED, the cristae structure cannot be resolved. Similarly, also TOMM20 is just one of the proteins sitting at the mitochondrial outer membrane and does not fully represent the complete membrane. Hence, we set-up CLEM with STED and TEM, to visualize the mitochondrial outer membrane and the cristae structure in a protein label-free manner. This permitted us to examine whether PLIN5 is present at the mitochondrial cristae and/or at the outer mitochondrial membrane. The TEM image clearly shows the mitochondrial cristae structure and the STED image shows PLIN5 and OXPHOS proteins in proximity (Fig. 3C). Interestingly, the overlay image clearly shows that PLIN5 is located outside the mitochondria (Fig. 3C) and in contrast to our previous immunogold TEM approach, not at the cristae or at the outer mitochondrial membrane.

Zooming in on the overview STED image of a longitudinal section of human skeletal muscle (Fig. 3D) identifies presence of PLIN5 in 3 pools; PLIN5 that is present in the cytosol but that is not bound to LDs nor to mitochondria (e.g., the encircled parts of Fig. 3E), PLIN5 in close association to mitochondria but not to LDs (e.g., see Fig. 3B) and a pool of

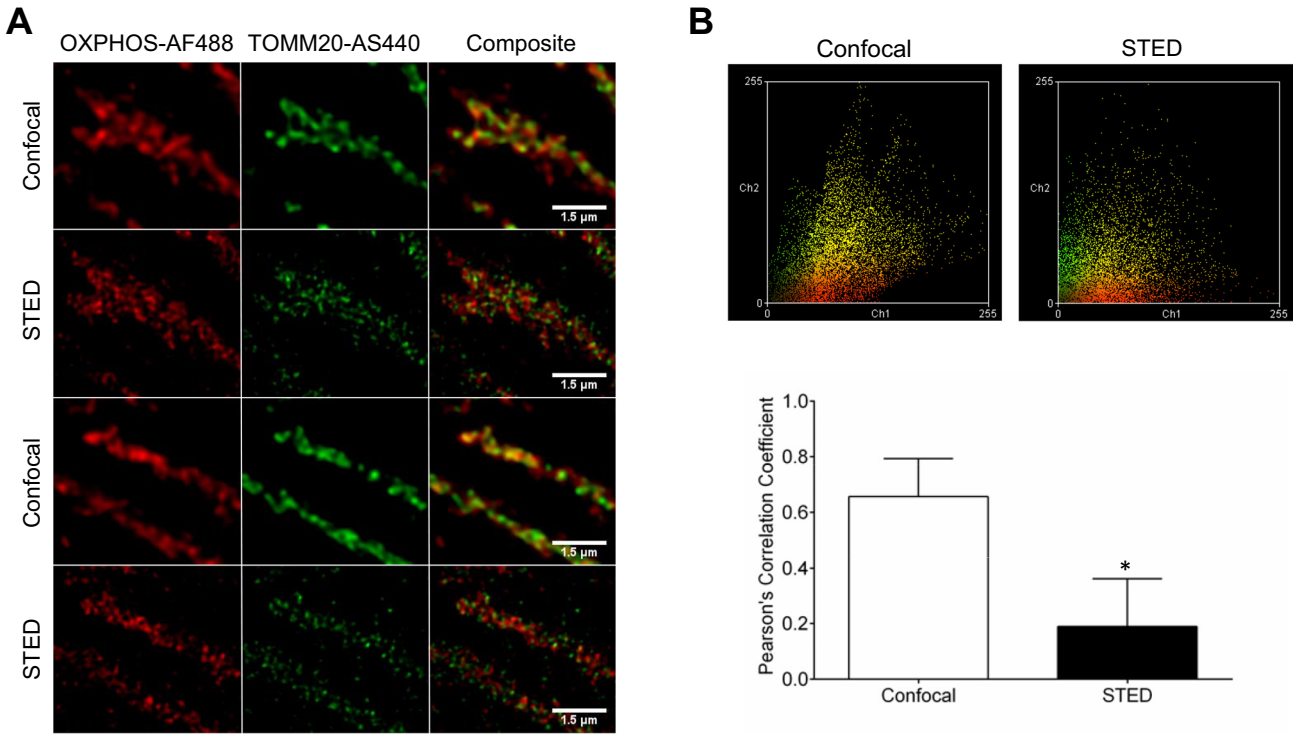

Fig. 2. Two-color STED imaging of near proximity mitochondrial proteins in human skeletal muscle. (A) Two-color confocal and STED imaging of OXPHOS-AF488 (red) and TOMM20-AS440 (green) in human skeletal muscle sections. (B) Plots of Pearson's correlation of pixel intensities of OXPHOS-AF488 and TOMM20-AS440 imaged with confocal (left-hand graph) and STED microscopy (right-hand graph). In the correlation plots Ch1 represents OXPHOS-AF488 and Ch2 represents TOMM20-AS440. The bar graph shows the Pearson's correlation coefficient quantification. In confocal images there appears to be partial overlap between the OXPHOS and TOMM20 proteins (as indicated by the yellow pixels in the image and by the Pearson's coefficient (0.657 ± 0.136, mean ± SD)), the higher resolving power of super-resolution microscopy indeed reveals differential location of OXPHOS and TOM20 proteins (Pearson's coefficient 0.189 ± 0.173, mean ± SD).

PLIN5 decorating the LD in a punctate fashion exactly at LD-mitochondria contact sites (Fig. 3E). The presence of cytosolic as well as PLIN5 on tethering sites of mitochondria to LD in human skeletal muscle was confirmed by CLEM (Fig. 3F). Although the previously reported location of PLIN5 on mitochondrial cristae was not confirmed using the STED based approach of the present study, we do see PLIN5 at the interaction sites of LDs and mitochondria.

3.4. On lipid droplets, PLIN2 and PLIN5 do not co-localize and present in a punctate fashion

Our third aim was to examine if PLIN2 and PLIN5 co-localize at the LD and to examine if these proteins envelop the entire LD as has been suggested by widefield and confocal microscopy, or if their distinct role in lipolysis is reflected in differential location at the LD. Our combined confocal and STED approach reveals that both PLIN2 and PLIN5 decorate the LDs in a dot-like fashion (Fig. 4A), for PLIN5 this was confirmed by CLEM (Fig. 3F). Upon performing colocalization analysis we observed a very low Pearson's correlation coefficient (0.117 ± 0.203, mean ± SD; data not shown). Since PLIN5 is not only present at the LD surface but on other subcellular locations as well, the Pearson's correlation coefficient can be biased by non-LD bound PLIN5 signal. Hence, we also created intensity profile plots at the outer contours of the LD as shown in Fig. 4B. In line with the Pearson's correlation coefficient, these intensity profile plots of PLIN2 and PLIN5 at the rim of the LDs indicated very limited overlap of the peaks of PLIN2 and PLIN5 (Fig. 4B). This suggests that PLIN proteins are spatially separated and are juxtaposing on the LD rather than co-localizing.

4. Discussion

Using two different super-resolution microscopy-based approaches we showed in human skeletal muscle sections that PLIN2 and PLIN5 do not co-localize but both locate to the LD surface in a punctate, dot-like, fashion rather than covering the entire LD as has previously been suggested. In contrast to PLIN2 which only localized to the LD surface, we identified three spatially separated pools of PLIN5; A cytosolic pool not associated with mitochondria or LDs, a pool in close proximity of mitochondria but not with LDs and a pool decorating the LD at the mitochondria-LD interface. These data could only be obtained upon developing and validating new protocols to stain LDs in human skeletal muscle sections. To this end, we imaged myocellular LDs with the blue LD dye MDH and employed correlative light-electron microscopy of STED images with transmission electron microscopy.

We applied STED microscopy to show that PLIN2 and PLIN5 coat the LD in a dot-like fashion rather than a rim-like structure as previously reported [5,8,14]. This is in line with recent observations of Dejgaard & Presley [29] who modelled that upon PLIN1-, PLIN2- and PLIN3-GFP transfection of HeLa cells, PLIN proteins do not completely cover the LD surface. The observed dot-like structure of PLIN2 and PLIN5 at the LD surface is in support of their different roles in lipolysis. The suggested role of PLIN2 in lipolysis is to shield the LD against lipolysis. Thus, in vitro and animal studies have shown overexpression of PLIN2 induces steatosis [9], compromises docking of ATGL to the LD and reduces lipolytic rate [11,30]. Conversely, PLIN2 knock-down in myotubes resulted in a lower lipid content [9,31] due to elevated LD hydrolysis, potentially via enriched docking of ATGL to the LD [31]. The STED based approach presented here -along with the observed dot-like location of PLIN2 at the LD surface and its physical disconnection from PLIN5- provides novel spatial information that is relevant to our

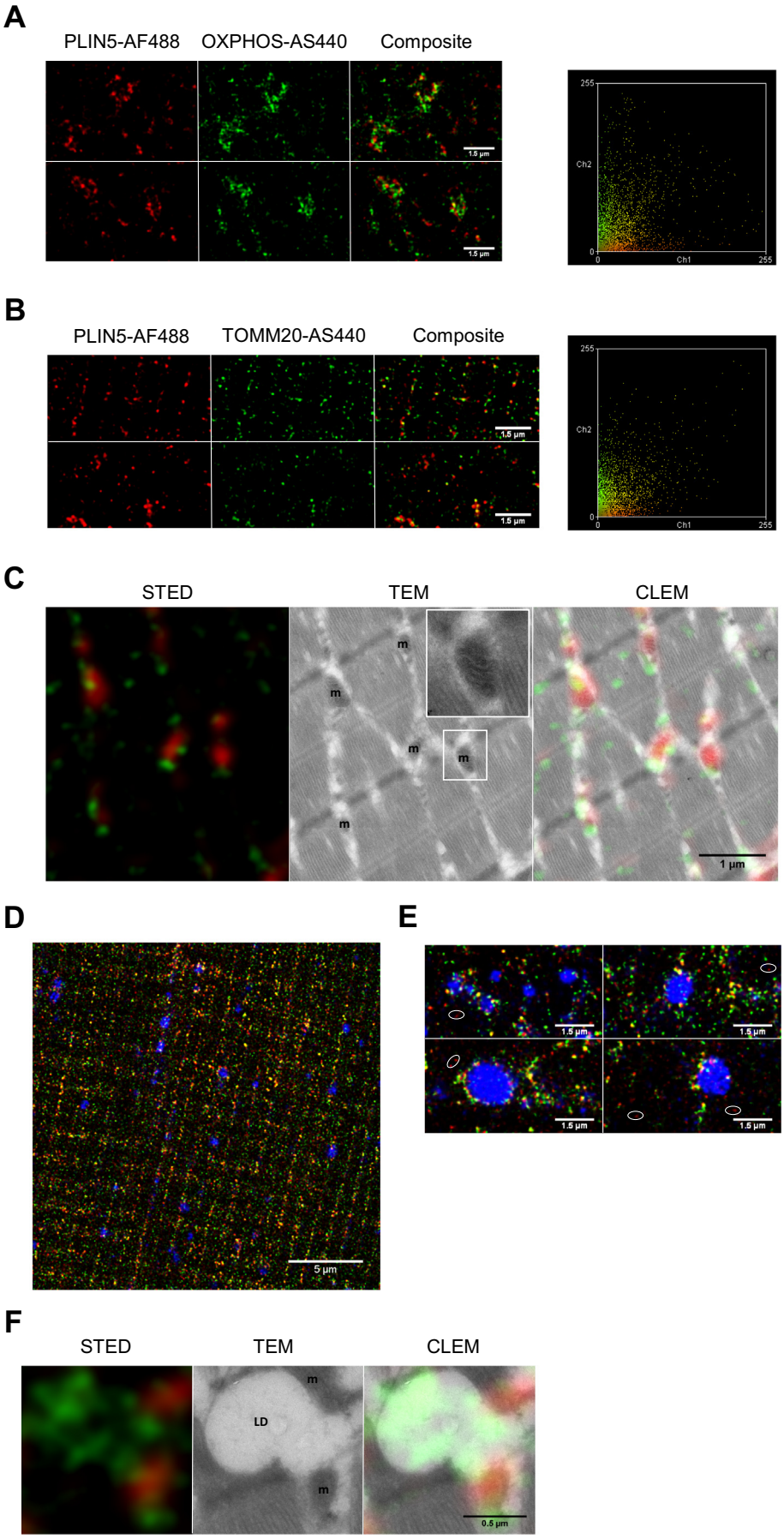

Fig. 3. PLIN5 is present at the mitochondrion-lipid droplet interface. (A) PLIN5 is in near vicinity of proteins at the inner mitochondrial membrane, PLIN5-AF488 is shown in red and OXPHOS-AS440 in green. Plot of Pearson's correlation coefficient analyses of pixel intensities of PLIN5-AF488 vs. OXPHOS-AS440 is shown on the right-hand side. Ch1 represents PLIN5-AF488 and Ch2 represents OXPHOS-AS440. (B) PLIN5 is in the near vicinity of TOMM20, a protein on the outer mitochondrial membrane (PLIN5-AF488 (red) and TOMM20-AS440 (green)). On the right-hand side a plot of the Pearson's correlation coefficient analysis of pixel intensities is shown. Ch1 represents PLIN5-AF488 and Ch2 represents TOMM20-AS440. (C) CLEM image consisting of a combined PLIN5 STED image and OXPHOS confocal (PLIN5 in green and OXPHOS in red) and a high-detailed TEM image of mitochondria (mitochondria marked by m). The insert shows a higher magnification of a mitochondrion where the cristae is clearly visible. See Supplemental Fig. S2 the workflow for alignment of the STED and TEM images. (D) Confocal imaging of MDH (blue) combined with STED imaging of TOMM20-AS440 (green). (E) Detailed image of randomly selected LDs, revealing PLIN5-AF488 (in red) at the LD-mitochondrial interface. Mitochondria are stained by TOMM20-AS440 (green). Not all PLIN5, however, is in direct vicinity of mitochondria (e.g., see the punctate PLIN5 staining in the encircled areas). (F) CLEM image consisting of a combined PLIN5 STED image and OXPHOS confocal (PLIN5 in green and OXPHOS in red) and a high-detailed TEM image of mitochondria and a lipid droplet (mitochondria marked by m, and lipid droplet by LD).

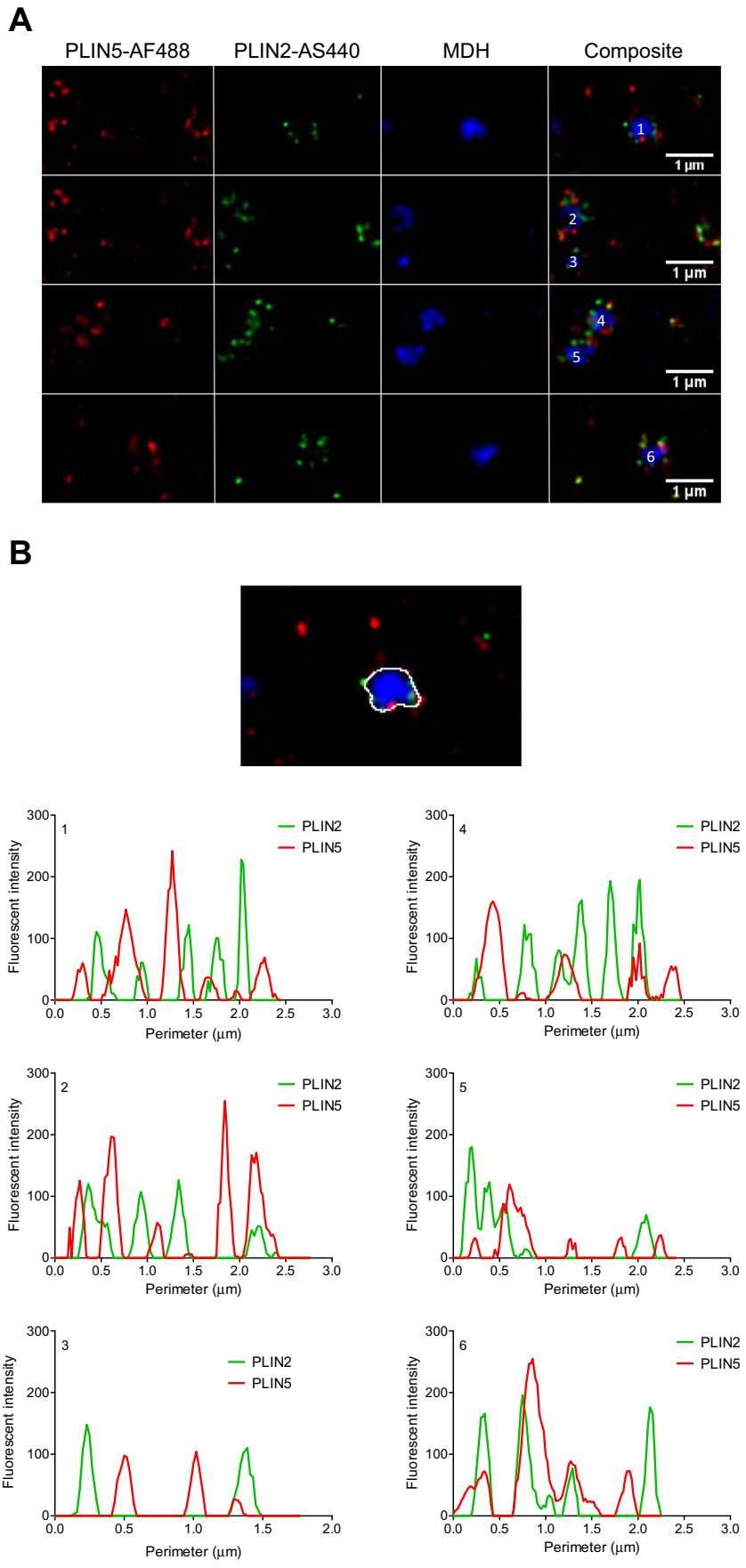

Fig. 4. PLIN5 is present as a dot-like structure on lipid droplets. (A) Combined confocal images of MDH (blue) and STED images of PLIN5-AF488 (red) and PLIN2-AS440 (green). PLIN5 and PLIN2 are juxtaposing a dot-like fashion on the surface of the lipid droplet. (B) Intensity plots of PLIN2 (green line) and PLIN5 (red line) of the outer contours (see white line in image above the graphs) of randomly selected LDs. The numbers in the composite image in panel A correspond with the numbers in the upper right corner of intensity profile plots of PLIN2 and PLIN5 in panel B. The peaks of the intensity profile plots of PLIN2 and PLIN5 are not overlapping, indicating spatially differential position of PLIN2 and PLIN5 on the LD surface.

understanding of how PLIN2 can recruit and dock proteins involved in lipolysis. This is particularly relevant in human studies where tagging proteins or genetically modifying protein content to examine protein function is not a feasible tool and endogenous proteins must be studied in their native environment.

Under basal conditions, PLIN5 decorating the LD serves as a lipolytic barrier [32–34]. Here, we identified three spatially separated pools of PLIN5, including a non-LD bound cytosolic pool. This is in line with previous findings of others performing PLIN5 overexpression in in vitro models [35,36]. Similar findings were observed in tissue from animals in sucrose density fractions [35]. Application of quantitative microscopy to examine the effect of physiological perturbations, further substantiates our observation of the existence of a non-LD bound pool of PLIN5. Thus, it was shown in human skeletal muscle that under conditions of elevated free fatty-acids levels, such as prolonged fasting [37] and intralipid infusion [7] the fraction of PLIN5 coated LDs increased significantly, without affecting total PLIN5 myocellular content. This indicates redistribution of PLIN5 from a non-LD bound pool to the LD surface. The redistribution of PLIN5 coincides with increases in LD size [7,37] and may serve to maintain the ratio of PLIN5 at the LD surface over LD volume to maintain lipolytic control. The existence of a LD-bound pool of PLIN5 fits this concept and explains the increase in LD size. The presence of PLIN5 at mitochondrial tethering sites, as observed in the present study, supports a role for PLIN5 in channeling fatty-acids derived from PKA-stimulated and PLIN5-facilitated LD lipolysis to fuel mitochondrial fat oxidation [14,34].

The observation of a pool of PLIN5 in close proximity with mitochondria not tethered to LDs is intriguing and not yet understood. Interestingly, it has recently been shown in brown adipose tissue (where the primary role of mitochondria is in heat- rather than ATP generation) that PLIN5 decorated LDs tether mitochondria to fuel triglyceride synthesis in the LD [38]. Conversely, in exercising muscle, LD derived fatty-acids fuel mitochondrial oxidation (for review see [4]). Physically connecting LDs with mitochondria associated with PLIN5 may promote LD-mitochondrial interaction and targeted delivery of fatty-acids to mitochondria for oxidation upon conditions of increased demand. This model fits with the observation that upon endurance exercise degradation of LDs is particularly prominent in PLIN5 coated LDs [6].

Thus, the spatially separated pools of PLIN5 may serve complimentary roles depending on the physiological condition. Under basal conditions and in the fed state, PLIN5 at the LD surface may control basal lipolysis and recruitment of cytosolic PLIN5 to the LD serves to maintain lipolytic control when excess fatty-acid availability makes the LD grow, while PLIN5 at mitochondria and LD-mitochondria interaction sites may serve to facilitate direct delivery of LD lipolysis released fatty-acids to mitochondria for oxidation.

While the role of PLIN2 and its interaction with lipolytic proteins is well established, exactly how PLIN5 is involved in regulating lipolysis is less well understood. Under lipogenic situations, PLIN5 interacts with CGI-58 [13,39], while upon lipolytic stimulation CGI-58 dissociates from PLIN5 and colocalizes with ATGL resulting in lipolysis [13]. It has, however, also been reported that PLIN5 binds to CGI-58 and ATGL [34], albeit in a mutually exclusive manner [40]. This may suggest a role for PLIN5 in facilitating colocalization of ATGL and CGI-58 upon lipolytic stimulation. Using two super-resolution imaging approaches, this is the first study to show that in sections of human skeletal muscle PLIN2 and PLIN5 do not co-localize at the LD surface, but are present at the LD surface in a juxtaposed fashion, which permits the spatial separation needed for selective docking of lipolytic proteins or blocking docking sites for these proteins. Thus, PLINs may regulate lipase access under a variety of lipolytic conditions.

(Dys)regulation of lipolysis is an important player -and hence target of treatment- in many metabolic disorders. A small molecule inhibitor of ATGL, Atglistatin has recently been shown to block ATGL activity by 95% in murine adipocytes. Disappointingly, however, this effect was almost completely absent in human adipocytes [41]. This stresses the notion to perform dedicated studies how native endogenous proteins are involved in human lipolysis.

The use of super-resolution microscopy has some limitations. STED microscopy reaches spatial resolutions closely to the size of the antibody-tree of the primary and secondary antibody. Thus, the spatial resolution might be limited by the use of antibodies. Unlike confocal microscopy, the commercially available pool of fluorescent probes that can be applied in STED is still limited (yet readily expanding). In our STED-system with one depletion laser we can only use two probes at the same time for STED imaging. STED microscopy can also be applied in live-cell imaging, with the advantage that processes and exogenous proteins (if tagged with a STED-able probe) can be monitored in real-time. The disadvantage, though, is that examination of lipolysis and endogenous proteins involved with STED is not yet feasible. Another disadvantage that can readily bias the interpretation of live-cell experiments is the phototoxicity that may come with the high power of the depletion laser of the STED system used. Despite these limitations, STED microscopy or other super-resolution microscopy techniques can be used to study subcellular protein localization in (human) tissues. Knowing the subcellular protein distribution provides valuable insights in the contribution of proteins to subcellular processes, like myocellular lipid droplet lipolysis.

5. Conclusion

To conclude, PLIN2 and PLIN5 coat the LD in a dot-like fashion, thus creating individual docking sites for e.g. lipases, rather than creating a lipolytic barrier as has previously been suggested. We also observed that PLIN2 and PLIN5 do not co-localize at the LD, but reside at the LD membrane juxtaposed. This provides the physical prerequisite for PLIN2 and PLIN5 to exert differential roles e.g., during basal or stimulated lipolysis. Super-resolution microscopy (STED and CLEM) revealed that, next to cytosolic localization of PLIN5, PLIN5 is present near mitochondria and at the interaction sites of mitochondria and the lipid droplet, supporting the notion that PLIN5 is involved in facilitating liberating fatty acids from the LD for mitochondrial fat oxidation. We foresee that application of the novel procedures outlined in this paper, along with the reported spatial distribution of PLIN2 and PLIN5 made, will contribute to our understanding of myocellular lipid droplet lipolysis under physiological and pathophysiological conditions.

Author contributions

Conceptualization, A.G. and M.K.C.H.; Methodology, A.G., S.D., H.J.H.K., C.L.I., M.A.M.J.Z., K.K. and M.K.C.H.; Investigation, A.G, S.D., H.J.H.K., G.S., H.D., and K.K.; Writing – Original Draft, A.G. and M.K.C.H. Writing – Review & Editing, S.D., H.J.H.K., G.S., H.D., C.L.I., M.A.M.J.Z. and K.K., Supervision, M.A.M.J.Z., K.K. and M.K.C.H.

Transparency document

The Transparency document associated with this article can be found, in online version.

Acknowledgements

We would like to thank Jacob Wefers, Dirk van Moorsel and Jan Hansen for providing the samples for the CLEM experiments.

A.G. and M.K.C.H. acknowledge financial support from the NanoNextNL, a micro and nanotechnology consortium of the Government of the Netherlands and 130 partners. A.G. is funded through an EFSD award supported by MSD. The work of S.D. is partly supported by Dutch Diabetes Research Foundation (grant DF 2014.00.1756) and by the NUTRIM—School for Nutrition, Toxicology

and Metabolism – NWO Graduate Program financially supported from Netherlands Organisation for Scientific Research (022.003.011). Projects of A.G., S.D. and M.K.C.H. are partly supported by the Netherlands Cardiovascular Research Initiative: an initiative with support of the Dutch Heart Foundation (CVON2014-02 ENERGISE). A grant for innovative research from the Netherlands Organisation for Scientific Research supports the current work of K.K. (VENI grant 863.14.003).

Declaration of interests

The authors declare no competing interests.

Appendix A. Supplementary data

Supplementary data to this article can be found online at https://doi.org/10.1016/j.bbalip.2018.08.016.

References

[1] A. Gemmink, B.H. Goodpaster, P. Schrauwen, M.K.C. Hesselink, Intramyocellular lipid droplets and insulin sensitivity, the human perspective, Biochim. Biophys. Acta 1862 (2017) 1242–1249.
[2] B.H. Goodpaster, J. He, S. Watkins, D.E. Kelley, Skeletal muscle lipid content and insulin resistance: evidence for a paradox in endurance-trained athletes, J. Clin. Endocrinol. Metab. 86 (2001) 5755–5761.
[3] L.J. van Loon, R. Koopman, R. Manders, W. van der Weegen, G.P. van Kranenburg, H.A. Keizer, Intramyocellular lipid content in type 2 diabetes patients compared with overweight sedentary men and highly trained endurance athletes, Am. J. Physiol. Endocrinol. Metab. 287 (2004) E558–E565.
[4] S. Daemen, N. van Polanen, M.K.C. Hesselink, The effect of diet and exercise on lipid droplet dynamics in human muscle tissue, J. Exp. Biol. (2018) 221.
[5] C.S. Shaw, S.O. Shepherd, A.J. Wagenmakers, D. Hansen, P. Dendale, L.J. van Loon, Prolonged exercise training increases intramuscular lipid content and perilipin 2 expression in type I muscle fibers of patients with type 2 diabetes, Am. J. Physiol. Endocrinol. Metab. 303 (2012) E1158–E1165.
[6] S.O. Shepherd, M. Cocks, K.D. Tipton, A.M. Ranasinghe, T.A. Barker, J.G. Burniston, A.J. Wagenmakers, C.S. Shaw, Sprint interval and traditional endurance training increase net intramuscular triglyceride breakdown and expression of perilipin 2 and 5, J. Physiol. 591 (2013) 19.
[7] S.O. Shepherd, J.A. Strauss, Q. Wang, J.J. Dube, B. Goodpaster, D.G. Mashek, L.S. Chow, Training alters the distribution of perilipin proteins in muscle following acute free fatty acid exposure, J. Physiol. 595 (2017) 5587–5601.
[8] K.T. Dalen, T. Dahl, E. Holter, B. Arntsen, C. Londos, C. Sztalryd, H.I. Nebb, LSDP5 is a PAT protein specifically expressed in fatty acid oxidizing tissues, Biochim. Biophys. Acta 1771 (2007) 210–227.
[9] M. Bosma, M.K. Hesselink, L.M. Sparks, S. Timmers, M.J. Ferraz, F. Mattijssen, D. van Beurden, G. Schaart, M.H. de Baets, F.K. Verheyen, S. Kersten, P. Schrauwen, Perilipin 2 improves insulin sensitivity in skeletal muscle despite elevated intramuscular lipid levels, Diabetes 61 (2012) 2679–2690.
[10] R. Minnaard, P. Schrauwen, G. Schaart, J.A. Jorgensen, E. Lenaers, M. Mensink, M.K. Hesselink, Adipocyte differentiation-related protein and OXPAT in rat and human skeletal muscle: involvement in lipid accumulation and type 2 diabetes mellitus, J. Clin. Endocrinol. Metab. 94 (2009) 4077–4085.
[11] L.L. Listenberger, A.G. Ostermeyer-Fay, E.B. Goldberg, W.J. Brown, D.A. Brown, Adipocyte differentiation-related protein reduces the lipid droplet association of adipose triglyceride lipase and slows triacylglycerol turnover, J. Lipid Res. 48 (2007) 2751–2761.
[12] H. Wang, U. Sreenivasan, H. Hu, A. Saladino, B.M. Polster, L.M. Lund, D.W. Gong, W.C. Stanley, C. Sztalryd, Perilipin 5, a lipid droplet-associated protein, provides physical and metabolic linkage to mitochondria, J. Lipid Res. 52 (2011) 2159–2168.
[13] M.A. Sanders, F. Madoux, L. Mladenovic, H. Zhang, X. Ye, M. Angrish, E.P. Mottillo, J.A. Caruso, G. Halvorsen, W.R. Roush, P. Chase, P. Hodder, J.G. Granneman, Endogenous and synthetic ABHD5 ligands regulate ABHD5-perilipin interactions and lipolysis in fat and muscle, Cell Metab. 22 (2015) 851–860.
[14] M. Bosma, R. Minnaard, L.M. Sparks, G. Schaart, M. Losen, M.H. de Baets, H. Duimel, S. Kersten, P.E. Bickel, P. Schrauwen, M.K. Hesselink, The lipid droplet coat protein perilipin 5 also localizes to muscle mitochondria, Histochem. Cell Biol. 137 (2012) 205–216.
[15] H. Wang, M. Lei, R.C. Hsia, C. Sztalryd, Analysis of lipid droplets in cardiac muscle, Methods Cell Biol. 116 (2013) 129–149.
[16] S.W. Hell, J. Wichmann, Breaking the diffraction resolution limit by stimulated emission: stimulated-emission-depletion fluorescence microscopy, Opt. Lett. 19 (1994) 780–782.
[17] T.A. Klar, S.W. Hell, Subdiffraction resolution in far-field fluorescence microscopy, Opt. Lett. 24 (1999) 954–956.
[18] T.A. Klar, S. Jakobs, M. Dyba, A. Egner, S.W. Hell, Fluorescence microscopy with diffraction resolution barrier broken by stimulated emission, Proc. Natl. Acad. Sci. U. S. A. 97 (2000) 8206–8210.
[19] S. Daemen, M.A. van Zandvoort, S.H. Parekh, M.K. Hesselink, Microscopy tools for the investigation of intracellular lipid storage and dynamics, Mol. Metab. 5 (2016) 153–163.
[20] H.J. Yang, C.L. Hsu, J.Y. Yang, W.Y. Yang, Monodansylpentane as a blue-fluorescent lipid-droplet marker for multi-color live-cell imaging, PLoS One 7 (2012) e32693.
[21] C.A. Schneider, W.S. Rasband, K.W. Eliceiri, NIH image to ImageJ: 25 years of image analysis, Nat. Methods 9 (2012) 671–675.
[22] F.G. Faas, M.C. Avramut, B.M. van den Berg, A.M. Mommaas, A.J. Koster, R.B. Ravelli, Virtual nanoscopy: generation of ultra-large high resolution electron microscopy maps, J. Cell Biol. 198 (2012) 457–469.
[23] E. Manders, F. Verbeek, J. Aten, Measurement of co-localization of objects in dual-colour confocal images, J. Microsc. 169 (1993) 375–382.
[24] P. Paul-Gilloteaux, X. Heiligenstein, M. Belle, M.C. Domart, B. Larijani, L. Collinson, G. Raposo, J. Salamero, eC-CLEM: flexible multidimensional registration software for correlative microscopies, Nat. Methods 14 (2017) 102–103.
[25] F. de Chaumont, S. Dallongeville, N. Chenouard, N. Herve, S. Pop, T. Provoost, V. Meas-Yedid, P. Pankajakshan, T. Lecomte, Y. Le Montagner, T. Lagache, A. Dufour, J.C. Olivo-Marin, Icy: an open bioimage informatics platform for extended reproducible research, Nat. Methods 9 (2012) 690–696.
[26] E. Currie, X. Guo, R. Christiano, C. Chitraju, N. Kory, K. Harrison, J. Haas, T.C. Walther, R.V. Farese Jr., High confidence proteomic analysis of yeast LDs identifies additional droplet proteins and reveals connections to dolichol synthesis and sterol acetylation, J. Lipid Res. 55 (2014) 1465–1477.
[27] B.H. Chen, H.J. Yang, H.Y. Chou, G.C. Chen, W.Y. Yang, Staining of lipid droplets with monodansylpentane, Methods Mol. Biol. 1560 (2017) 231–236.
[28] C. Greggio, P. Jha, S.S. Kulkarni, S. Lagarrigue, N.T. Broskey, M. Boutant, X. Wang, S. Conde Alonso, E. Ofori, J. Auwerx, C. Canto, F. Amati, Enhanced respiratory chain supercomplex formation in response to exercise in human skeletal muscle, Cell Metab. 25 (2017) 301–311.
[29] S.Y. Dejgaard, J.F. Presley, New method for quantitation of lipid droplet volume from light microscopic images with an application to determination of PAT protein density on the droplet surface, J. Histochem. Cytochem. 66 (2018) 447–465.
[30] S. Kaushik, A.M. Cuervo, Degradation of lipid droplet-associated proteins by chaperone-mediated autophagy facilitates lipolysis, Nat. Cell Biol. 17 (2015) 759.
[31] Y.Z. Feng, J. Lund, Y. Li, I.K. Knabenes, S.S. Bakke, E.T. Kase, Y.K. Lee, A.R. Kimmel, G.H. Thoresen, A.C. Rustan, K.T. Dalen, Loss of perilipin 2 in cultured myotubes enhances lipolysis and redirects the metabolic energy balance from glucose oxidation towards fatty acid oxidation, J. Lipid Res. 58 (2017) 2147–2161.
[32] N.M. Pollak, M. Schweiger, D. Jaeger, D. Kolb, M. Kumari, R. Schreiber, S. Kolleritsch, P. Markolin, G.F. Grabner, C. Heier, K.A. Zierler, T. Rulicke, R. Zimmermann, A. Lass, R. Zechner, G. Haemmerle, Cardiac-specific overexpression of perilipin 5 provokes severe cardiac steatosis via the formation of a lipolytic barrier, J. Lipid Res. 54 (2013) 1092–1102.
[33] C. Laurens, V. Bourlier, A. Mairal, K. Louche, P.M. Badin, E. Mouisel, A. Montagner, A. Marette, A. Tremblay, J.S. Weisnagel, H. Guillou, D. Langin, D.R. Joanisse, C. Moro, Perilipin 5 fine-tunes lipid oxidation to metabolic demand and protects against lipotoxicity in skeletal muscle, Sci. Rep. 6 (2016) 38310.
[34] H. Wang, M. Bell, U. Sreenivasan, H. Hu, J. Liu, K. Dalen, C. Londos, T. Yamaguchi, M.A. Rizzo, R. Coleman, D. Gong, D. Brasaemle, C. Sztalryd, Unique regulation of adipose triglyceride lipase (ATGL) by perilipin 5, a lipid droplet-associated protein, J. Biol. Chem. 286 (2011) 15707–15715.
[35] S.R. Bartholomew, E.H. Bell, T. Summerfield, L.C. Newman, E.L. Miller, B. Patterson, Z.P. Niday, W.E.t. Ackerman, J.T. Tansey, Distinct cellular pools of perilipin 5 point to roles in lipid trafficking, Biochim. Biophys. Acta 1821 (2012) 268–278.
[36] J.R. Skinner, T.M. Shew, D.M. Schwartz, A. Tzekov, C.M. Lepus, N.A. Abumrad, N.E. Wolins, Diacylglycerol enrichment of endoplasmic reticulum or lipid droplets recruits perilipin 3/TIP47 during lipid storage and mobilization, J. Biol. Chem. 284 (2009) 30941–30948.
[37] A. Gemmink, M. Bosma, H.J. Kuijpers, J. Hoeks, G. Schaart, M.A. van Zandvoort, P. Schrauwen, M.K. Hesselink, Decoration of intramyocellular lipid droplets with PLIN5 modulates fasting-induced insulin resistance and lipotoxicity in humans, Diabetologia 59 (2016) 1040–1048.
[38] I.Y. Benador, M. Veliova, K. Mahdaviani, A. Petcherski, J.D. Wikstrom, E.A. Assali, R. Acin-Perez, M. Shum, M.F. Oliveira, S. Cinti, C. Sztalryd, W.D. Barshop, J.A. Wohlschlegel, B.E. Corkey, M. Liesa, O.S. Shirihai, Mitochondria bound to lipid droplets have unique bioenergetics, composition, and dynamics that support lipid droplet expansion, Cell Metab. 27 (2018) 869–885.e866.
[39] J.G. Granneman, H.P. Moore, E.P. Mottillo, Z. Zhu, Functional interactions between Mldp (LSDP5) and Abhd5 in the control of intracellular lipid accumulation, J. Biol. Chem. 284 (2009) 3049–3057.
[40] J.G. Granneman, H.P. Moore, E.P. Mottillo, Z. Zhu, L. Zhou, Interactions of perilipin-5 (Plin5) with adipose triglyceride lipase, J. Biol. Chem. 286 (2011) 5126–5135.
[41] M. Schweiger, M. Romauch, R. Schreiber, G.F. Grabner, S. Hutter, P. Kotzbeck, P. Benedikt, T.O. Eichmann, S. Yamada, O. Knittelfelder, C. Diwoky, C. Doler, N. Mayer, W. De Cecco, R. Breinbauer, R. Zimmermann, R. Zechner, Pharmacological inhibition of adipose triglyceride lipase corrects high-fat diet-induced insulin resistance and hepatosteatosis in mice, Nat. Commun. 8 (2017) 14859.